Tropical–Extratropical Teleconnections in Boreal Summer: Observed Interannual Variability*

QINGHUA DING+

Department of Meteorology, School of Ocean and Earth Science and Technology, University of Hawaii at Manoa, Honolulu, Hawaii

BIN WANG

Department of Meteorology, and International Pacific Research Center, School of Ocean and Earth Science and Technology, University of Hawaii at Manoa, Honolulu, Hawaii

JOHN M. WALLACE

Department of Atmospheric Sciences, University of Washington, Seattle, Washington

GRANT BRANSTATOR

NCAR,# Boulder, Colorado

(Manuscript received 15 January 2010, in final form 28 October 2010)

ABSTRACT

Maximum covariance analysis is performed on the fields of boreal summer, tropical rainfall, and Northern Hemisphere (NH) 200-hPa height for the 62-yr period of record of 1948–2009. The leading mode, which appears preferentially in summers preceding the peak phases of the El Niño–Southern Oscillation (ENSO) cycle, involves a circumglobal teleconnection (CGT) pattern in the NH extratropical 200-hPa height field observed in association with Indian monsoon rainfall anomalies. The second mode, which tends to occur in summers following ENSO peak phases, involves a western Pacific–North America (WPNA) teleconnection pattern in the height field observed in association with western North Pacific summer monsoon rainfall anomalies. The CGT pattern is primarily a zonally oriented wave train along the westerly waveguide, while the WPNA pattern is a wave train emanating from the western Pacific monsoon trough and following a great circle. The CGT is accompanied by a pronounced tropical–extratropical seesaw in the zonally symmetric geopotential height and temperature fields, and the WPNA is observed in association with hemispherically uniform anomalies. These ENSO-related features modulate surface air temperature in both the tropics and extratropics. ENSO also affects the wave structure of the CGT and WPNA indirectly, by modulating the strengths of the Indian and western North Pacific monsoons. Linear barotropic mechanisms, including energy propagation and barotropic instability of the basic-state flow, also act to shape and maintain the CGT. The implications of these findings for seasonal prediction of the NH extratropical circulation are discussed.

1. Introduction

Skillful seasonal prediction of the Northern Hemisphere (NH) extratropical circulation, especially over land areas, could be of great utility and economic value. Current climate models have reasonable skill in forecasting El Niño–Southern Oscillation (ENSO) events but only very limited skill in forecasting the NH summer-mean extratropical circulation (Wang et al. 2008). Hence, it is conceivable that an improved understanding of the global teleconnections associated with anomalous latent heat release in the tropics could lead to improved prediction of the

* International Pacific Research Center Publication Number 745 and School of Ocean and Earth Science and Technology Publication Number 8066.

+ Current affiliation: University of Washington, Seattle, Washington.

The National Center for Atmospheric Research is sponsored by the National Science Foundation.

Corresponding author address: Dr. Qinghua Ding, Sciences and Quaternary Research Center, Department of Earth and Space, University of Washington, Seattle, WA 98195.
E-mail: qinghua@uw.edu

DOI: 10.1175/2011JCLI3621.1

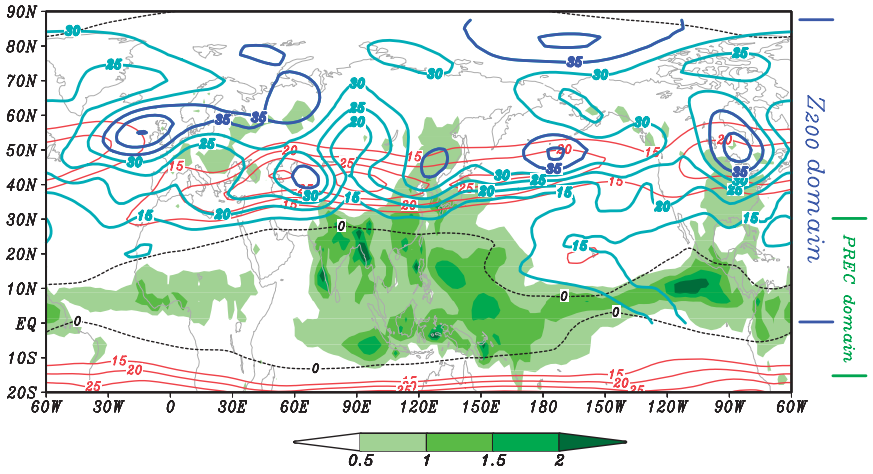

FIG. 1. Standard deviation of seasonal-mean PREC rainfall (shading, interval = 0.5 mm day^{-1}) and 200-hPa NH geopotential height (Z_{200}) anomalies (blue contours, 5-m contour interval, centers with maximum >35 m highlighted by dark blue), together with isotachs of climatological mean JJA 200-hPa zonal wind indicating the location of the jet stream (red contours, 5 m s^{-1} contour interval, values >15 m s^{-1} only) for the period 1948–2009. The black dotted line indicates the zero line of climatological-mean JJA 200-hPa zonal wind. The latitudinal domains for MCA are indicated by blue and green lines along the right axis.

interannual variability of the extratropical summertime circulation.

The major NH teleconnection patterns during boreal winter were first recognized nearly three decades ago (e.g., Wallace and Gutzler 1981; Horel 1981; Barnston and Livezey 1987). The tropical Northern Hemisphere (Barnston and Livezey 1987) and Pacific–East Asian teleconnection patterns (Wang et al. 2000) capture the dominant tropical–extratropical teleconnections associated with the mature phase of ENSO. In addition, Branstator (2002) found a wintertime circumglobal waveguide pattern in the NH extratropical circulation based on the analysis of the internal variability of observational data and model output. This pattern exhibits a strong zonal wavenumber 5 component with peak amplitude around the latitude of the Asian jet stream. It does not exhibit well-defined nodes and antinodes in the zonal direction. Chen (2002) found evidence that it may be linked to tropical forcing.

During the boreal summer, the NH westerly jet weakens and shifts poleward (Fig. 1), resulting in weaker teleconnection patterns, and the tropical SST anomalies also tend to be weaker than during winter because ENSO episodes usually reach their mature stage toward the end of the calendar year (Rasmusson and Carpenter 1982). Hence, the ENSO-related tropical–extratropical linkage is less clear than during winter. Conversely, it is conceivable that the summer monsoons over southern Asia, the western North Pacific (WNP), Mexico, and North Africa could be capable of influencing the extratropical circulation by virtue of their proximity to the subtropical jet stream. Barnston and Livezey (1987) recognized three significant NH summertime teleconnection patterns: North Atlantic Oscillation, a subtropical zonal mode, and a single-centered Asian monsoon mode. A Eurasian teleconnection pattern oriented along the westerly jet stream was also pointed out (Joseph and Srinivasan 1999; Lu et al. 2002; Enomoto et al. 2003). However, none of these patterns has explicitly been linked to ENSO.

Tropical–extratropical teleconnections have also been invoked in numerous studies of climatic extreme events, such as the 1988 drought and the 1993 flood across North America (Trenberth et al. 1988; Trenberth and Branstator 1992; Lau and Peng 1992; Trenberth and Guillemot 1996; Ting and Wang 1997). These studies showed evidence that the North American summer circulation is sensitive to SST anomalies over both the tropical and midlatitude North Pacific. Teleconnection patterns linking convective heating anomalies over the western North Pacific with circulation anomalies over East Asia and downstream over North America have been documented by Nitta (1987), Lau (1992), Wang et al. (2001), and Lau and Weng (2002). Hoerling and Kumar (2003) and Lau et al. (2005) also suggested that the Indo–western Pacific SST warming could generate a belt of positive, zonally symmetric, upper-level geopotential height that could induce anomalous warmth and dryness.

Based on an analysis of monthly-mean anomaly data, Ding and Wang (2005; hereafter DW05) found a boreal summer stationary circumglobal teleconnection (CGT) pattern in the NH. In contrast to the boreal winter

circumglobal waveguide pattern, the centers of action of the summer CGT pattern tend to be phase locked, with preferred longitudes over the eastern Atlantic, west central Asia, northeastern Asia, the central Pacific, and central Canada. The geographically phase-locked patterns observed during June, August, and September are very similar; however, the pattern in July exhibits shorter wavelengths in the Pacific–North America sector. It was shown that the CGT pattern is closely associated with Indian summer monsoon (ISM) variability and may also be indirectly influenced by ENSO during periods of strong ISM–ENSO interactions.

The boreal summer CGT pattern has been the topic of subsequent investigations focusing on meteorological (Blackburn et al. 2008) and climatic aspects (Li et al. 2008; Rajeevan and Sridhar 2008; Yadav 2009a,b; Lin 2009; Yasui and Watanabe 2010) and practical forecast applications (Yang et al. 2009).

While some progress has been made in the study of boreal summertime teleconnections, many aspects of the tropical–extratropical teleconnections remain to be elucidated. For instance, is the CGT pattern evident in seasonal mean summertime anomalies? How prominent is the CGT pattern in the interannual variability of the extratropical NH circulation? Is the CGT pattern evident in the teleconnections between NH 200-hPa geopotential height and tropical rainfall, and are there other significant teleconnection patterns involving these fields besides the CGT pattern? How do these patterns relate to ENSO, the boreal summer monsoons, and the internal dynamic stability of the extratropical basic-state flow? The present study aims at addressing these questions.

Since some aspects of the subseasonal (monthly anomalies within the season June–September) and intraseasonal variations of the CGT over Eurasia have been investigated in our previous works (DW05; Ding and Wang 2007, 2009), here we focus our attention on year-to-year variations in the tropical NH–extratropical connections in seasonal mean [June–August (JJA)] anomalies. Basing this study on seasonal-mean fields, rather than monthly-mean fields, enables us to focus on the interannual variability. It also provides an indication of how well a dynamically based seasonal prediction model might be expected to perform.

2. Data and analysis method

a. Data

Three datasets are extensively used in our observational analyses: 1) National Centers for Environmental Prediction–National Center for Atmospheric Research (NCEP–NCAR) reanalysis monthly data for the period 1948–2009 (Kalnay et al. 1996); 2) monthly global SST for the period 1948–2009 from the National Oceanic and Atmospheric Administration's (NOAA) extended reconstructed SST (ERSST) version 3 (Smith et al. 2008); and 3) the NOAA global monthly precipitation reconstruction (PREC) dataset (Chen et al. 2004). Two additional monthly datasets were used to investigate the influence of the extratropical teleconnection patterns on precipitation and surface air temperature over the NH land areas: the NOAA precipitation reconstruction data over land (PREC/L) compiled by Chen et al. (2002), and the land surface air temperature dataset compiled by the Climatic Research Unit (CRU) (Mitchell and Jones 2005). Both datasets are available for the period 1948–2009 on a 0.5° latitude/longitude grid. The all-India rainfall index (AIRI) for the period 1948–2009 was used as a measure of the intensity of the ISM (Parthasarathy et al. 1994). Monsoon circulation indices defined by Wang et al. (2001) were used to quantify interannual fluctuations of the ISM and the western North Pacific summer monsoon (WNPSM).

Most of the global precipitation datasets are based on satellite measurements, which are available for only the three most recent decades. A notable exception is the PREC rainfall dataset, which extends from 60°S to 75°N and covers both land and ocean for the 62-yr record 1948–2009 (Chen et al. 2004). The land rainfall in PREC was produced by optimal interpolation of gauge observations of monthly precipitation at more than 17 000 stations. The oceanic PREC fields are projections of historical gauge observations over islands and land areas onto empirical orthogonal functions (EOFs) derived from satellite observations for later years (1979–98). PREC is able to retrieve the precipitation anomaly associated with ENSO and other large-scale circulation patterns reasonably well over most of the tropical and subtropical oceanic areas (Chen et al. 2004).

b. Statistical tests

To focus on year-to-year variations, the interannual component of the data is used. The long-term trend and decadal variations with periods longer than 8 yr are removed using Fourier harmonic analysis of the seasonal-mean (JJA) anomalies. The numbers of degrees of freedom for each variable (geopotential height, rainfall, and surface temperature) at each grid point were estimated using the method described by Chen (1982). Since the lag-1 autocorrelation of these 2–8-yr filtered variables is very small, the seasonal-mean values for successive years are statistically independent and the assumption of 1 degree of freedom per year is appropriate. With this number of degrees of freedom, a correlation coefficient with a magnitude greater than about 0.25 is statistically significant at the 95% confidence level.

In addition, the significance of correlation coefficients was retested through the 1000 Monte Carlo simulation procedure (Wilks 1995; Livezey and Chen 1983). In all cases studied here, we found that the 95% confidence level determined by this Monte Carlo technique corresponded to a lower value of the correlation coefficient than 0.25. Thus, in the following sections, correlations with absolute values of coefficients exceeding 0.25 are shown and regarded as significantly different from zero.

c. *Analysis methods*

The main statistical tools utilized in this study include maximum covariance analysis (MCA), EOF analysis, and compositing. MCA extracts the modes that explain the greatest squared covariance between two different fields (Bretherton et al. 1992; Wallace et al. 1992). We use MCA to capture the dominant related modes between the NH extratropical 200-hPa height field and tropical precipitation, a measure of the tropical forcing. The square root of cosine of latitude weighting was used in computing the covariance matrix. The analysis was performed on both raw and standardized fields, and results were found to be very similar. In the composite analysis, the Student's *t* test (Wilks 1995) was used to assess statistical significance.

3. Tropical–extratropical teleconnections

To provide an indication of the interannual variability, Fig. 1 shows the standard deviation of the 62-yr (1948–2009) record of JJA precipitation and 200-hPa height. The most prominent feature in the 200-hPa height field, with a standard deviation $\sigma > 40$ m, is located over the northeast Atlantic and western Europe near the exit region of the North Atlantic jet. Other local maxima, with $\sigma > 35$ m, are observed over central Asia, northeastern China, the central North Pacific, and central Canada—all of which are closely associated with the major summertime jet streams along 40°–50°N. The most intense tropical rainfall variability ($\sigma > 1$ mm day^{-1}) is observed over the summer monsoon regions (southern Asia, the Philippine Sea, and off the coast of Mexico), over equatorial Indonesia and in the Pacific ITCZ.

a. *The leading modes of covariability between tropical precipitation and 200-hPa height*

Now we apply MCA to the fields of precipitation over the entire tropical region of 15°S–30°N and 200-hPa height over the entire NH for each summer (JJA) during the period of 1948–2009. Very similar results (not shown) were obtained when the analysis was performed on the same tropical rainfall field paired with the 200-hPa height field poleward of 20°N.

The first MCA mode (M1) explains about 47% of the total covariance between the two fields, and the correlation between the associated expansion coefficient time series is 0.78. The rainfall pattern (Fig. 2a) resembles the characteristic ENSO signature, represented here with negative polarity, with reduced rainfall centered over the equatorial Pacific near the date line and enhanced rainfall over most of the remainder of the tropics. The corresponding 200-hPa height pattern is dominated by positive anomalies in the belt centered around 40°N. Embedded within this ring of above-normal heights is a circumpolar wave train, with anomalous anticyclonic circulations centered over the eastern Atlantic, central Asia, northeastern China, the central Pacific, just off the California coast, and over central Canada. The positions of the anticyclones are associated with features of the JJA upper-tropospheric jet stream except for the one off the California coast. Negative height anomalies prevail over much of the tropical belt. The only notable feature in high latitudes is the negative height anomaly over the Gulf of Alaska. The circumpolar wave train pattern in M1 resembles the CGT pattern identified in DW05. In particular, the North America sector of this wave train resembles an anomalous circulation pattern favoring extreme drought events over the United States. (Trenberth et al. 1988; Trenberth and Branstator 1992; Trenberth and Guillemot 1996). The high correlation between the expansion coefficient time series of M1 in the 200-hPa height field and AIRI (Table 1) is indicative of a tight relationship between the ISM and the extratropical circulation pattern of M1.

The second mode (M2) shown in Fig. 2b explains 25% of the squared covariance fraction (SCF) between the two fields and has a correlation coefficient of 0.73 between its expansion coefficient time series. The rainfall pattern associated with this mode exhibits positive loadings in a band extending from the Philippine Sea eastward across the Pacific between 5° and 20°N. Negative rainfall anomalies cover the southern portion of the warm pool, the Maritime Continent, and Central America. Most of the Asian monsoon region tends to be dry, but the pattern is patchy. The corresponding 200-hPa height pattern is biased toward negative anomalies over the NH as a whole, and it exhibits a complex wave train pattern extending from eastern Siberia, across the North Pacific and North America. In contrast to the CGT pattern in M1, the circulation pattern in M2 is more regional and more complex. It exhibits some similarity to the teleconnection pattern associated with the WNPSM identified by Nitta (1987) and Wang et al. (2001). Thus, this 200-hPa height wave pattern is more closely related to the diabatic heating over the WNP and to the intensity of the WNPSM (Table 2), although its connection with the WNPSM is weaker than the CGT–ISM connection. Wang et al. (2001) have shown

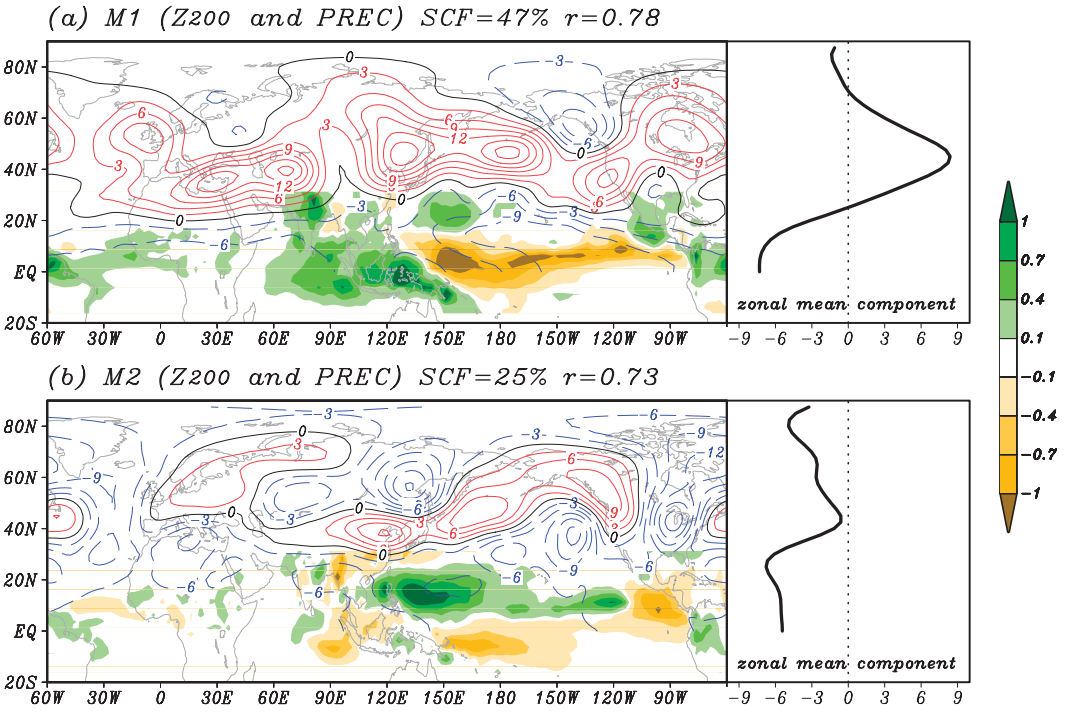

FIG. 2. (a) M1 and (b) M2 between 200-hPa height (contours, interval = 3 m) and PREC tropical rainfall (shading, interval = 0.3 mm day^{-1}). SCF and the temporal correlation coefficient (r) between two expansion coefficient time series are indicated on the top of each panel. Singular vectors are scaled by one standard deviation of the corresponding expansion coefficient time series, and these represent typical amplitudes. The zonally averaged 200-hPa height anomalies are shown on the right side of the panels.

that this teleconnection pattern links rainfall variations in the western Pacific monsoon trough and climate anomalies over the Great Plains of the United States. The wave train in the height pattern exemplified by M2 will be referred to as the western Pacific–North America (WPNA) teleconnection pattern.

b. *The zonally symmetric components of the teleconnection modes*

The response to a stationary heat source is typically viewed as assuming the form of a wave train (e.g., Hoskins and Karoly 1981). The two leading MCA modes in Fig. 2 exhibit not only wave train structures but also zonally symmetric features. M1 exhibits a meridional seesaw structure between the tropics and extratropics with a node along ~20°N (Fig. 2a), while M2 is biased toward height anomalies of the same sign throughout the NH, including the tropics (Fig. 2b). These zonally symmetric signals, which are clearly evident in the insets on the right-hand side of Fig. 2, are far too strong to be interpreted as residuals of wave train patterns. Mechanisms that might be responsible for these annular features are considered later in this study.

4. Impacts of M1 and M2 on extratropical climate

a. *Vertical structure of the leading modes and their impacts on surface temperature and rainfall*

To reveal the vertical structure of the wave trains in the two leading MCA modes, we calculated correlation coefficients between the expansion coefficient time series of M1 and M2 with time series of 200-hPa (Figs. 3a and 3c), 500-hPa height (not shown), and 700-hPa height (Figs. 3b and 3d). For the CGT pattern (M1), all but one of the circulation centers of the wave train exhibit a nearly equivalent barotropic structure. The exception is the anticyclonic

TABLE 1. Correlation coefficients between the 200-hPa height expansion coefficient time series of M1 and seasonal mean AIRI, Indian monsoon index (IMI), PC of EOF2 of the hemispheric 200-hPa height field (Fig. 4c), and the Niño-3 index for 62-yr period of record 1948–2009. IMI is defined as the meridional shear of the 850-hPa westerlies; i.e., the 850-hPa zonal winds averaged over the southern region (5°–15°N, 40°–80°E) minus that averaged over the northern region (20°–30°N, 70°–90°E) (Wang et al. 2001).

	AIRI	IMI	EOF2	Niño-3
M1	0.62	0.53	0.90	−0.76

TABLE 2. Correlation coefficients between the 200-hPa height expansion coefficient time series of M2 and the seasonal mean WNP monsoon index (WNPMI), PC of EOF1 of the hemispheric 200-hPa height field (Fig. 4a), and the Niño-3 index for the 62-yr period of record 1948–2009. WNPMI is defined as the meridional shear of the 850-hPa westerlies, i.e., the 850-hPa zonal winds averaged over the southern region (5°–15°N, 100°–130°E) minus that averaged over the northern region (20°–30°N, 110°–140°E) (Wang et al. 2001).

	WNPMI	EOF1	Niño-3
M2	0.45	0.91	−0.20

cell over central Asia, which shows an indication of a phase reversal between the upper and lower troposphere, suggestive of the possible influence of diabatic heating associated with Indian monsoon precipitation.

The tropical–extratropical dipole and the barotropic centers of action in the CGT pattern (M1) exert an influence on the temperature and precipitation fields. When M1 is present in its positive polarity, the extratropical continents tend to be anomalously warm and the tropics anomalously cool, as shown in Fig. 3a. The extratropical warmth is most pronounced in the belt around 40°N. The wave component of the CGT pattern gives rise to a distinctive pattern of regional rainfall variations along its path, as shown in Fig. 3b.

The most noteworthy feature of the corresponding correlation maps for M2 is the uniformly negative 200- and 700-hPa height, and surface temperature correlations in the tropics and the prevalence of negative correlations throughout the entire domain of the analysis (Figs. 3c and 3d). The hemispheric cooling in association with the positive polarity of M2 masks any wavelike signature of the WPNA pattern that might be present. This mode is weakly correlated with rainfall on a global scale but shows some related rainfall signal over North America (Fig. 3d).

b. *Major modes of interannual variability of the NH 200-hPa geopotential height*

To place M1 and M2 in the context of their contributions to the variance of the 200-hPa height field, EOF analysis was performed on the same dataset. EOFs 1 and 2 closely resemble the 200-hPa fields in M2 and M1, respectively (Fig. 4). The correlation coefficients between their respective expansion coefficients are in excess of 0.9 (Tables 1 and 2). Hence, it can be said that M1 and M2 correspond closely to the leading modes of variability of the 200-hPa height field, which together account for roughly one-third of the total variance and an even larger fraction in the regions of strongest interannual variability (Fig. 1). EOF 1 and M2 account for about 70% of the variance of 200-hPa height at most tropical grid points.

The frequent occurrence of CGT along the jet possibly contributes to the formation of strong variability centers at these specific locations. In particular, it appears that

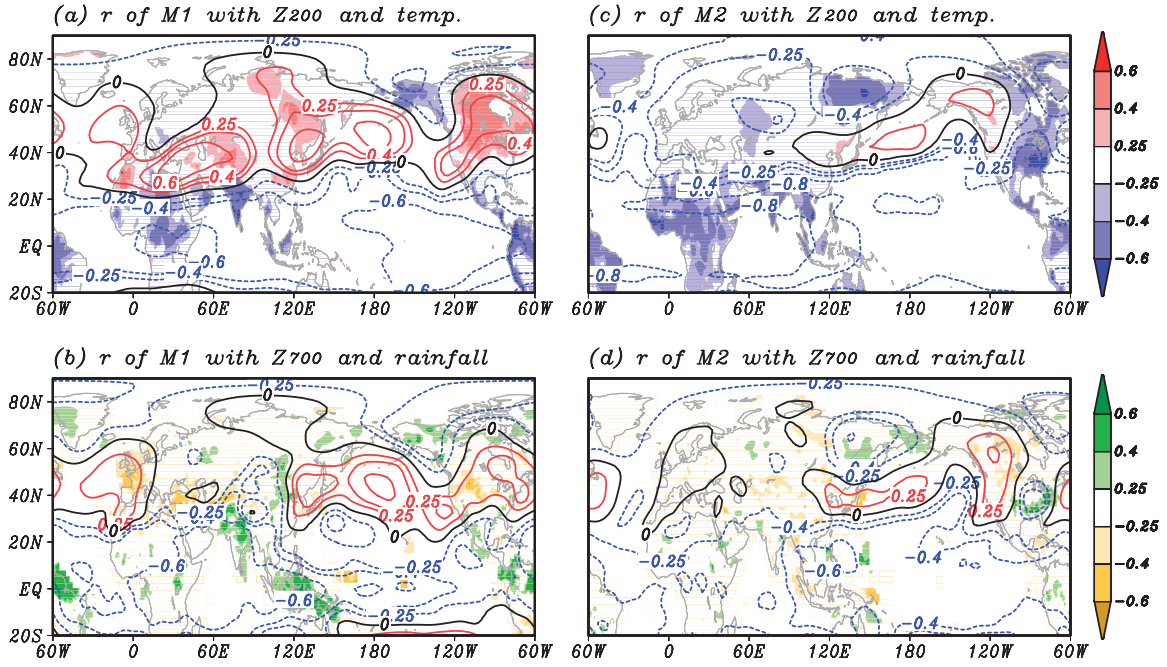

FIG. 3. Correlation coefficient between expansion coefficient time series of (a),(b) M1 and (c),(d) M2 with (a),(c) 200-hPa height (contours) and CRU land surface temperature anomalies (shading) and (b),(d) 700-hPa height (contours) and land precipitation (PREC/L) anomalies (shading). Contours are at 0, ±0.25, ±0.4, ±0.6, and ±0.8.

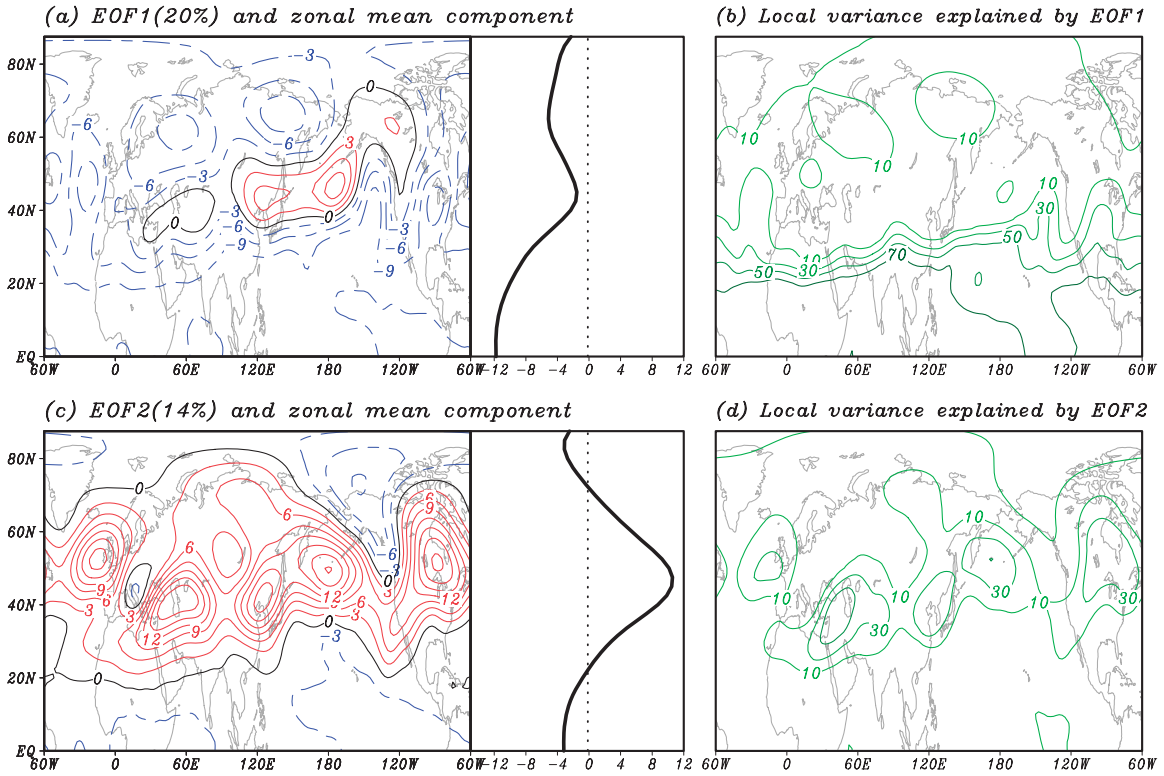

FIG. 4. (a),(b) EOF1 and (c),(d) EOF2 based on analysis of a 62-yr (1948–2009) record of seasonal-mean NH 200-hPa height anomalies. (a),(c) Spatial pattern of the EOF with zonally averaged 200-hPa height displayed at the right side. (b),(d) Ratio of square of the EOF amplitude to the total variance at each grid (contour interval = 20%). The EOFs modes have been scaled by one standard deviation of the corresponding principal components (PCs; contour interval = 3 m).

the CGT pattern, with its close relationship with tropical rainfall variability and the NH jet streams, could play an important role in conveying the influence of tropical thermal forcing to the extratropics.

5. The influence of ENSO

a. Role of ENSO in modulating M1 and M2

The results shown in Fig. 2 suggest that the precipitation patterns associated with the two MCA modes are closely associated with ENSO. The dominance of these two singular value decomposition (SVD) modes (47% + 25%) in the MCA may be due to the dominance of the ENSO signal in the variability of tropical rainfall. To explore this possibility, the evolution of the SST pattern from the preceding winter {December–February [DJF(0)]} to the subsequent winter [DJF(1)] is documented on the basis of compositing. Positive and negative years are classified on the basis of the expansion coefficient of the height pattern in M1, with one standard deviation as a threshold value. We found that the composites for contrasting polarities of M1 and M2 are nearly mirror images of one another. Accordingly, we use the differences between positive and negative M1 (M1+ minus M1−) composites as a measure of the SST anomalies associated with M1, and similarly for M2.

The SST evolution associated with M1+ (Figs. 5a–5c) shows what appears to be a developing La Niña event, proceeding from no signal in the preceding winter to the mature phase in the following winter. In contrast, the SST evolution associated with M2+ is indicative of decay from a La Niña peak in the previous DJF to no signal in the following DJF (Figs. 5d–5f; Table 2).

The M1 DJF(1) SST anomalies (Fig. 5c) bear a striking relationship to the M2 DJF(0) SST anomalies (Fig. 5d), suggesting that M1+ and M2+ (and M− and M2 −) are very likely to occur in consecutive summers, the first preceding and the second following the peak phase of an El Niño or La Niña event. That the expansion coefficients of M1 and M2 are well correlated ($r = 0.56$) with M1 leading M2 by a year, the DJF Niño-3 index is correlated with the previous JJA value of the M1 expansion coefficient time series ($r = -0.67$), and the following JJA value of the M2 time series ($r = -0.68$) lends further credence to this interpretation and to the notion that M1 and M2 exhibit some degree of predictability by virtue

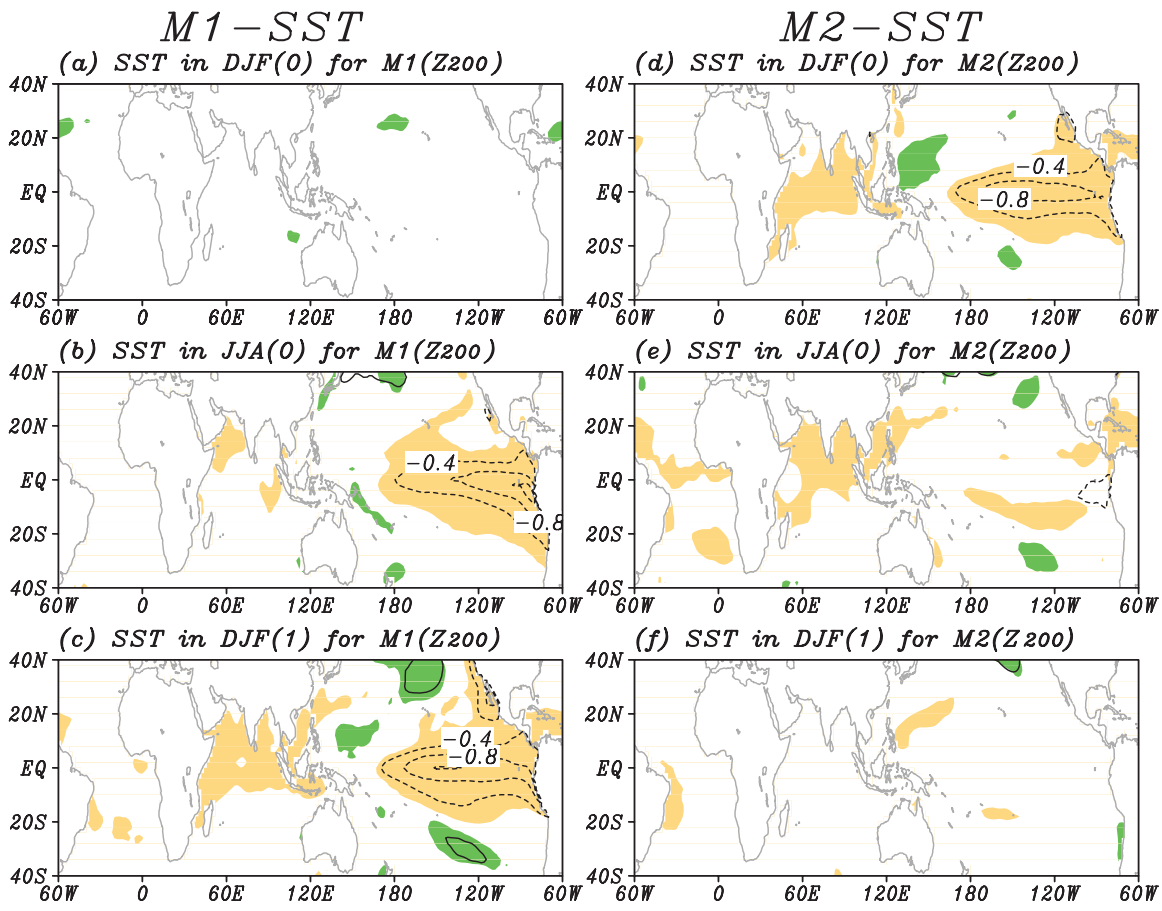

FIG. 5. Composite difference between SST anomalies in years with positive and negative polarities of the 200-hPa height expansion coefficient time series of (a)–(c) M1 and (d)–(f) M2 (contour interval = 0.4°C). Time sequence in the composites depict (a),(d) the previous DJF, (b),(e) the concurrent JJA, and (c),(f) the subsequent DJF. Shading denotes regions in which the difference is significant at or above the 95% confidence level: green is positive and brown is negative.

of their relationship to the ENSO cycle. In the summer of the year in which El Niño or La Niña is developing, the CGT pattern is favored. During the summer of the following year, in which El Niño or La Niña is decaying, the WPNA pattern is favored. Compositing with M1 and M2 as the reference time series indicates that the distribution of tropical convection and the extratropical response exhibit distinctive patterns in developing summers and decaying summers of ENSO events.

Now we perform the compositing analysis in the reciprocal or inverse manner, using DJF SST anomalies averaged over the equatorial central-eastern Pacific (5°S–5°N, 180°E–80°W) as the reference time series with one standard deviation as a cutoff for defining warm (El Niño) and cold (La Niña) events (Table 3). Despite the observed asymmetry between warm and cold phases of the ENSO cycle, with SST anomalies being stronger during the warm phase (Burgers and Stephenson 1999), the basic structure of composites for warm and cold events is quite symmetric on a global scale. For the sake of brevity, we show only the difference between cold and warm composites (referred to as "La Niña minus El Niño"). We denote the year in which the ENSO-related anomalies are amplifying as year 0 and the following (decaying) year as year 1. Thus, the summer of the amplifying year is symbolized as JJA(0) and the summer of the following year as JJA(1).

Composites of tropical rainfall and NH extratropical circulation anomalies in JJA(0) and JJA(1) exhibit

TABLE 3. El Niño and La Niña events during 1948–2009 used in compositing analysis in Figs. 6 and 7. ENSO events are defined in accordance with the DJF SST anomalies averaged over the equatorial central-eastern Pacific with a threshold of one standard deviation. Only the calendar years of the December of these events are listed in the table.

El Niño	1957, 1965, 1972, 1982, 1986, 1997, 2009
La Niña	1949, 1955, 1967, 1970, 1973, 1975, 1984, 1988, 1995, 1999, 2005, 2007

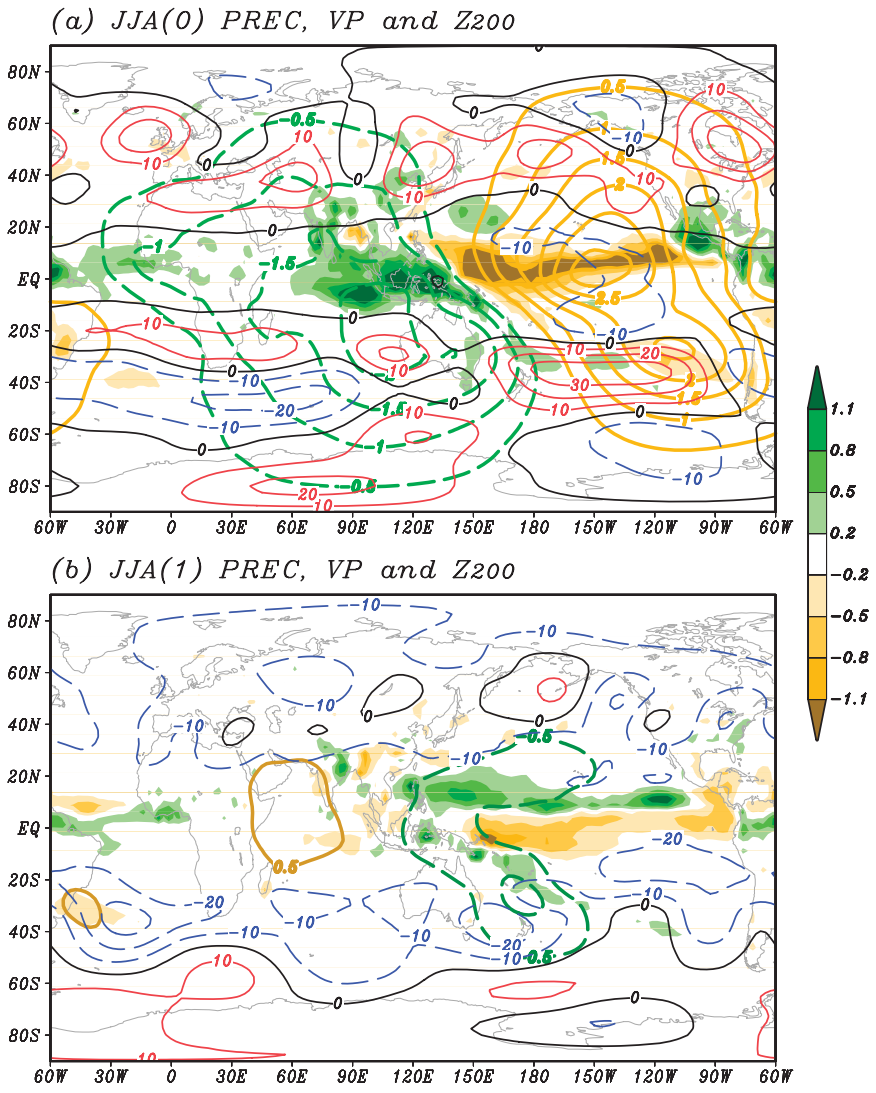

FIG. 6. Composite difference of seasonal-mean 200-hPa height (red and blue contours, interval = 10 m), 200-hPa velocity potential (green and brown contours, interval = 0.5 × 10^6 m^2 s^{-1}) and PREC precipitation (shading, interval = 0.3 mm day^{-1}) between La Niña and El Niño years (La Niña − El Niño) during (a) the boreal summer preceding the La Niña/El Niño peak and (b) the boreal summer succeeding it. The composite difference was divided by 2. La Niña/El Niño years are defined as years in which DJF SST over the equatorial central-eastern Pacific exceeds one standard deviation (Table 3).

considerable similarity to the M1 and M2 composites, respectively (Fig. 6). The patterns in the tropics and extratropics of both hemispheres in JJA(0) are much stronger than those in JJA(1). The JJA(0) pattern (depicted here for the case of a La Niña event; Fig. 6a) is marked by suppressed rainfall over the equatorial Pacific and enhanced rainfall over most of the remainder of the tropics. The enhancement of the rainfall is especially notable over the equatorial Indian Ocean, along the Atlantic ITCZ, and in the subtropical summer monsoon areas of India and Mexico. The ENSO composite in Fig. 6a replicates all the major features of tropical rainfall of M1 (Fig. 2a). The subtropical features may be particularly important in this respect because of their proximity to the jet stream. The JJA(0) 200-hPa height pattern in the SH is equally strong and contains the signature of the Pacific–South America (PSA) teleconnection pattern (Karoly 1989).

The JJA(1) tropical rainfall anomalies are weaker and not as well organized on a planetary scale, as reflected in the much weaker anomalies in the field of velocity potential in Fig. 6b. There is little evidence of an extratropical response in the 200-hPa height field in either hemisphere.

That the tropical rainfall anomalies in the JJA(0) composite are so much stronger and better organized than those in the JJA(1) composite is at least, in part, because of the strong seasonality of the ENSO cycle, as reflected in the much stronger autocorrelation of ENSO indices from JJA to the subsequent DJF than from DJF to the subsequent JJA (Goswami and Shukla 1991; Barnston et al. 1994; Balmaseda et al. 1994; Xue et al. 1994; Latif et al. 1998, Torrence and Webster 1998). Yet, despite its relative weakness, the JJA(1) pattern of tropical rainfall bears a strong resemblance to the tropical rainfall pattern in M2. Another factor that may contribute to the almost complete lack of an extratropical 200-hPa height response to the JJA(1) tropical rainfall is the fact that the rainfall anomalies in this season are mainly confined within the tropical western and central Pacific between 20°–20°S, and they have little influence on the summer monsoons.

From these compositing results, it is evident that M1 and the CGT pattern are strongly influenced by the ENSO cycle in the JJA of the year of a developing El Niño or La Niña event. The tropical rainfall pattern of M2 resembles that observed in JJA following a peak El Niño or La Niña event, but there appears to be little or no direct connection between the ENSO cycle and the WPNA pattern in the 200-hPa height field.

b. *Impact of ENSO on the zonally symmetric component of atmospheric variability*

The zonally symmetric component of the atmospheric variability observed in association with ENSO and ENSO-related SST anomalies over the Indo–western Pacific and the tropical Atlantic has been discussed in studies of Yulaeva and Wallace (1994), Hoerling et al. (2001), Kumar et al. (2001), Schubert et al. (2002), Hoerling and Kumar (2003), Kumar and Hoerling (2003), Seager et al. (2003), and Lau et al. (2005). Because the zonally symmetric response to ENSO is symmetric about the equator and occurs in all seasons (Seager et al. 2003), we apply the compositing methodology used by Kumar and Hoerling (2003) to examine the month-to-month development of zonally averaged global geopotential height anomalies during the composite life cycle of the ENSO events defined in the previous subsection (Table 3). Figures 7a and 7b show a composite 2-yr cycle of zonal-mean height at 200 and 700 hPa from January (0) to December (1) for the composite La Niña − El Niño together with the meridionally averaged SST anomaly in the equatorial belt, 10°S–10°N (Fig. 7c).

During a La Niña event, the geopotential height at upper-tropospheric levels decreases in response to the suppressed convection and cooling over the central Pacific. This regional forcing generates equatorial Kelvin and Rossby waves that spread the tropospheric cooling signature eastward and westward, respectively, eventually leading to a more uniform cooling over the entire global tropics, giving rise to a lagged response of the entire tropical atmosphere to ENSO forcing, which was extensively studied by Yulaeva and Wallace (1994), Kumar and Hoerling (2003), and some of the other studies cited above.

A striking feature of the tropical tropospheric response to a La Niña forcing is the gradual widening of negative zonally averaged geopotential height in the tropics. In early summer of year 0, the zonal band of tropical negative height covers only the tropical (20°S–20°N) belt. This band widens to around 35°S–35°N in D(0)JF(1) and 60°N–60°S in JJA(1) (Figs. 7a and 7b). An out-of-phase relationship between negative height anomalies in the tropics and positive height in the extratropics is evident in both hemispheres from JJA(0) to April(1). As the ENSO forcing weakens around early spring of year 1, this tropical–extratropical seesaw structure begins to disappear, and by a few months later the band of negative height anomalies in the tropics spreads to cover most of the globe (Figs. 6b and 7a). A similar evolution is observed at 700 hPa but with weaker intensity.

During the years in which El Niño-related SST anomalies are amplifying, the zonally symmetric, meridional seesaw pattern between the tropics and extratropics may be explained by the mechanism proposed by Seager et al. (2003) that invokes the effects of the fluxes of zonal momentum by transient eddies. For example, during La Niña events, negative SST anomalies in the equatorial central Pacific lead to a spatially uniform cooling of the entire tropics, which in turn leads to changes in the eddy-driven mean meridional circulation that induce extratropical warming, as reflected in positive extratropical geopotential height perturbations amplifying with height. As the eddy-induced extratropical warming dies away in the spring of year 1, it seems reasonable that the mean meridional circulation should return to normal, so that the only remnant of the La Niña event is the thermodynamically induced cooling, which by this time has spread nearly pole-to-pole but remains strongest at lower latitudes. The Indo–western Pacific SST anomalies succeeding the extreme of the ENSO cycle also contribute to the extratropical NH zonally symmetric geopotential height anomalies during JJA(1) (Hoerling and Kumar 2003; Kumar and Hoerling 2003; Lau et al. 2005).

ENSO exhibits a significant zonally symmetric signature in its own right, which also contributes to zonally symmetric anomalies observed in association the CGT and WPNA patterns, as depicted in Fig. 2.

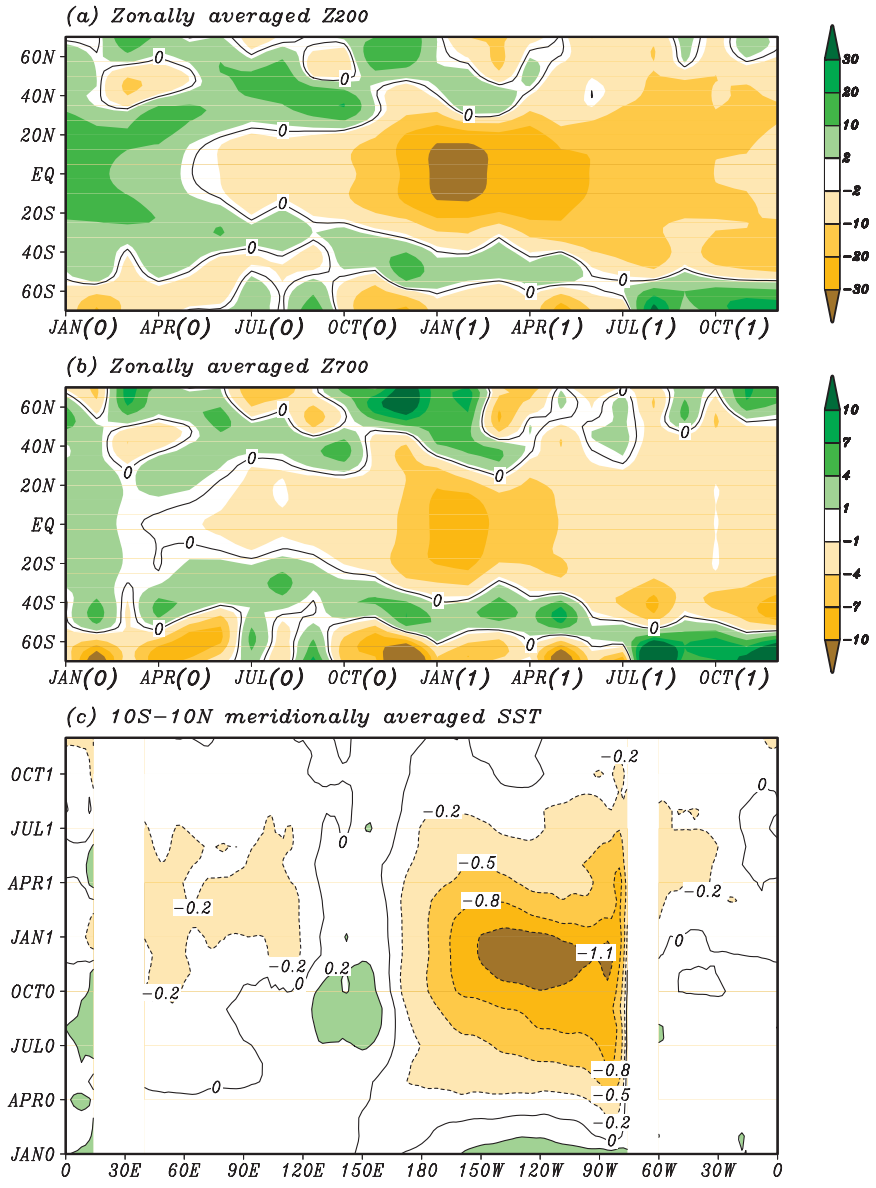

FIG. 7. Lead–lag composite difference of monthly zonally averaged (a) 200-hPa height (shading), (b) 700-hPa height (shading), and (c) 10°N–10°S meridionally averaged SST anomalies between La Niña event and El Niño years (La Niña − El Niño) from Jan(0) to Dec(1). Composite difference and definition of La Niña/El Niño years are as in Fig. 6.

6. Impact of the monsoons on the wave components of tropical–extratropical teleconnections

We now turn our attention to the zonally asymmetric component of the CGT and WPNA patterns, with special emphasis on how they are forced by tropical heating. As shown in Table 1, both ENSO and the ISM are significantly correlated with the CGT. It is known that ENSO can influence the ISM (e.g., Sikka 1980; Shukla and Paolino 1983). Hence, it is conceivable that ENSO-related tropical heating anomalies force the CGT by way of the ISM. Composite charts of JJA 200-hPa height and tropical rainfall anomalies shown in Fig. 8 support this interpretation. During years of strong ISM but weak ENSO-related rainfall anomalies (Fig. 8a), the wave component of the CGT remains intact from central Asia to North America; however, the zonally symmetric component of the pattern shows a different structure from that of CGT. In contrast, in years when ISM rainfall is near

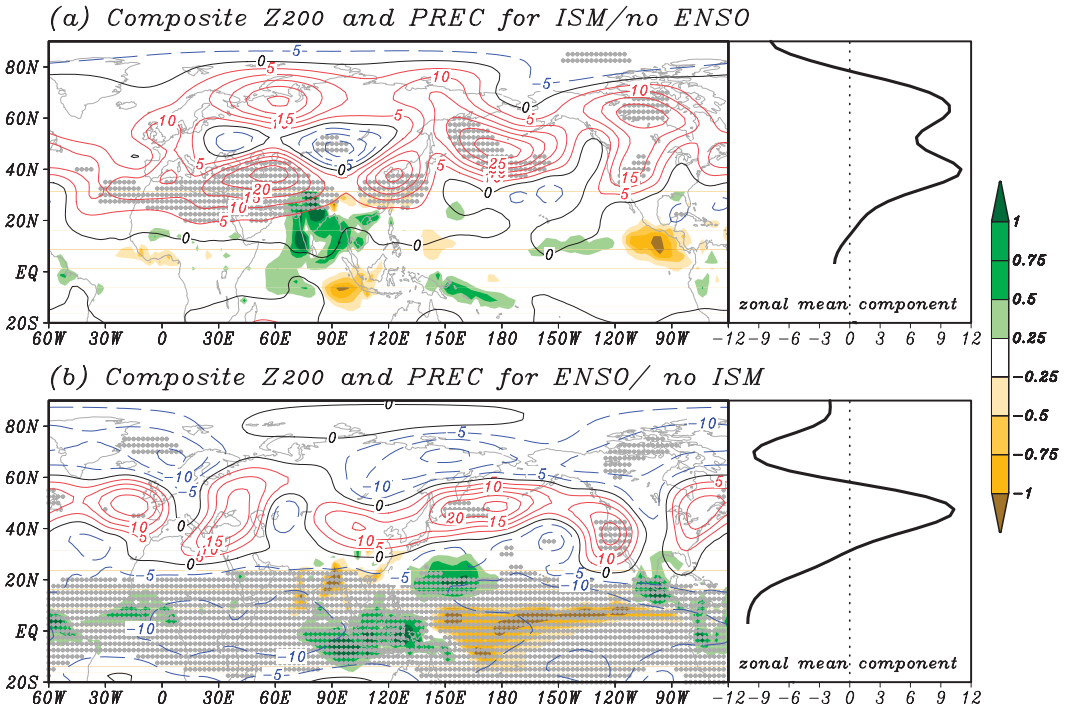

FIG. 8. Composite difference of seasonal 200-hPa height (contour interval = 5 m) and PREC precipitation (shading, mm day^{-1}) between (a) strong ISM years (1961, 1967, 1980, 1994, 2001, and 2003) and weak ISM years (1962, 1974, 1979, 1992, and 2002) with respect to AIRI, when ENSO is normal; (b) La Niña years (1949, 1955, 1981, 1985, 1996, and 1999) and El Niño years (1963, 1976, 1982, 1991, and 1997) with respect to equatorial central-eastern Pacific SST when the ISM is normal. The zonally averaged 200-hPa height anomalies are shown at the right side. La Niña − El Niño composite in (b) is used to facilitate the comparison with the MCA results. Composite differences have been divided by 2. Dots mark 200-hPa height differences that are significant at or above the 95% confidence level. ENSO definitions in accordance with equatorial central-eastern Pacific SST, and the ISM definitions in accordance with AIRI. Abnormal years are defined as years in which the standardized indices exceed std dev = 0.8 in absolute value, and the remaining years are classified as normal years.

normal but ENSO-related tropical rainfall anomalies are strong (Fig. 8b), the extratropical 200-hPa height field exhibits zonally elongated anomalies in the belt along ~45°N and a tropical–extratropical seesaw pattern. The zonally asymmetric part of the CGT is therefore more robustly linked to the ISM than to ENSO.

The structure of M1 (Fig. 2a) is also suggestive of a relationship between the CGT wave pattern and precipitation from rainfall anomalies over the WNP north of 15°N, Mexico, and North Africa. The correlations with rainfall in these regions are weaker and more localized than those associated with the ISM, but the results shown in Fig. 9 suggest that the anomalies associated with the Mexican monsoon contribute to the center of action of the CGT off the coast of California.

Rainfall anomalies over the WNP are larger, more robust, and located closer to the equator during the summer following a peak in the ENSO cycle than in the preceding summer (Wang et al. 2000; Lau and Nath 2003). Hence, the influence of rainfall anomalies over the WNP on the extratropical WPNA pattern is also of interest. The pattern formed by correlating the 200-hPa height field with rainfall over the WNP south of 20°N (8.75°–21.25°N, 128.75°–163.75°E) exhibits a structure similar to the WPNA pattern in M2 (Fig. 9e). Thus, it appears that the wave train structure of the WPNA pattern can be largely explained by the tropical forcing in the WNPSM.

7. Internal variability of the extratropical circulation

The segment of the CGT pattern that extends from the central North Pacific across North America resembles the most unstable normal mode of the June basic state calculated by Lau and Peng (1992). Given that the mean flow in June is quite similar to the summer-mean state, this result suggests that the structure and prominence of the CGT may be a consequence of those dynamical processes that are represented in the model used by Lau and Peng (1992), which is based on the linearized nondivergent

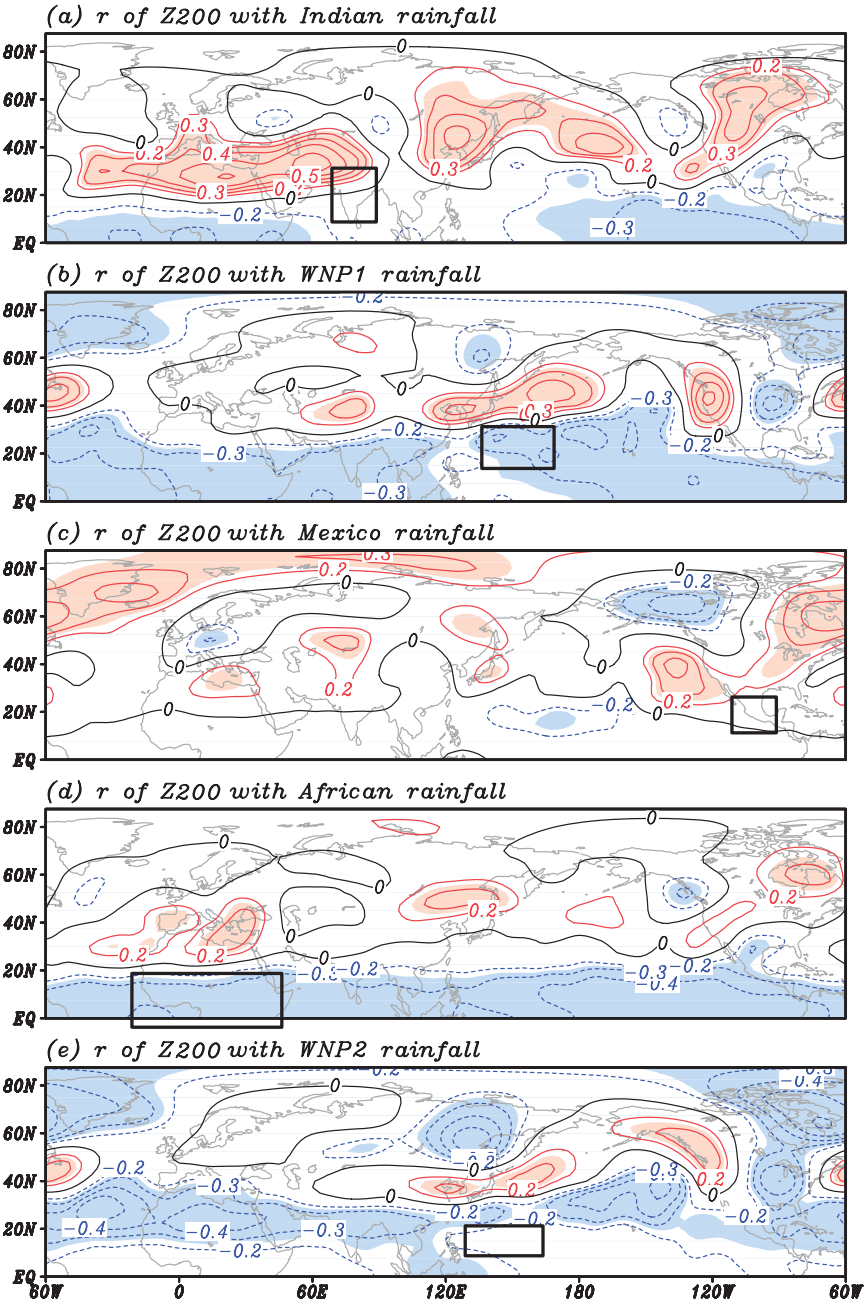

FIG. 9. Correlation of 200-hPa height with seasonal-mean rainfall over (a) India (8.75°–31.25°N, 68.75°–88.75°E), (b) the WNP1 region (13.75°–31.25°N, 136.25°–168.75°E), (c) Mexico (11.25°–26.25°N, 111.25°–91.25°W), (d) Africa (3.75°S–18.75°N, 21.25°W–46.25°E), and (e) WNP2 (8.75°–21.25°N, 128.75°–163.75°E). Red contours denote positive correlations, and blue contours denote negative correlations. Shading denotes correlations that are significant at or above the 95% confidence level (±0.25). Contours are at 0, ±0.25, ±0.3, ±0.4, ±0.5, and ±0.6. The solid box denotes the region over which the rainfall is averaged. WNP1 indicates the region over which significant M1-related rainfall anomalies occur in the summers preceding the peak phase of the ENSO cycle. WNP2 indicates the region over which significant M2-related rainfall anomalies occur in the summer following the peak phase.

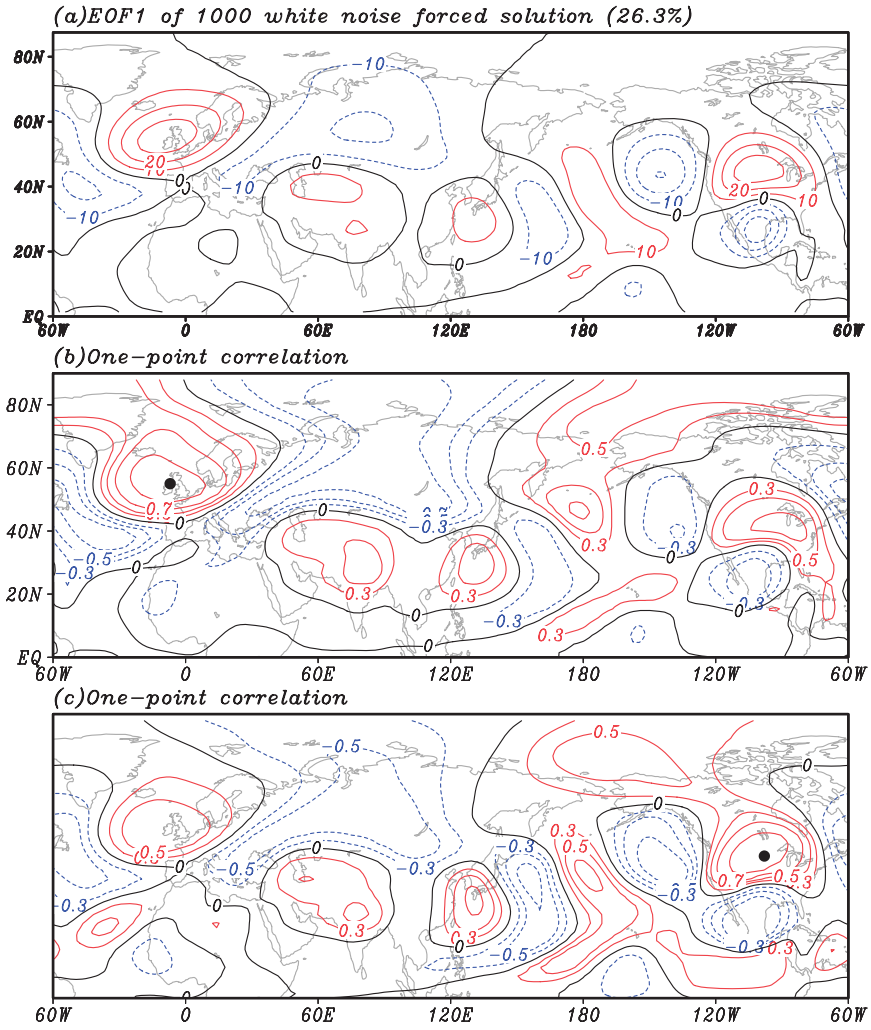

FIG. 10. The first EOF of the 1000 barotropic model response (streamfunction) to global white-noise forcing. (a) EOF1 explains 26.3% of total variance. (b) One-point correlation maps of 1000 streamfunction response for strong positive loading of EOF1 at northeast Atlantic (52.5°–57.5°N, 7.5°–2.5°W) and (c) North America (42.5°–47.5°N, 102.5°–97.5°W), indicated by black dots. Red contours indicate positive correlations, and blue contours negative correlations. Contour interval is 10^6 m^2 s^{-1} in (a) and 0, ±0.3, ±0.5, ±0.7, and ±0.9 in (b) and (c).

barotropic vorticity equation. To test this possibility, we have taken this model and linearized it about the 200-hPa climatological-mean JJA flow. To determine which long-lasting perturbation structures would tend to be prominent solely as a result of their interactions with the mean state (Branstator 1990), we have forced the model with 1000 different distributions of steady vorticity forcing. Each of these distributions was formed by random draws from a uniform distribution, so that the forcing is white in space (see the appendix for details about the model). Using randomly forced solutions rather than normal modes to explore the effects of linear dynamics on perturbations has the advantage of allowing us to analyze the behavior of the linear model in exactly the same fashion as we have analyzed the observational fields. And we need make no assumptions as to the relative contribution of various normal modes to the statistical behavior of the linear model.

Figure 10a shows the first EOF of streamfunction for the 1000 steady solutions we have calculated. Even though the forcing we have employed has no preferred structures, the resulting solutions are highly organized, with 26.3% of the variance being explained by this one pattern. The most prominent feature of EOF1 is a zonal wavenumber 5 global wave train circumscribing the entire NH, with the strongest amplitude cells over the northeast Atlantic and North America. This global wave train represents the preferred pattern of variability of the JJA state and shows

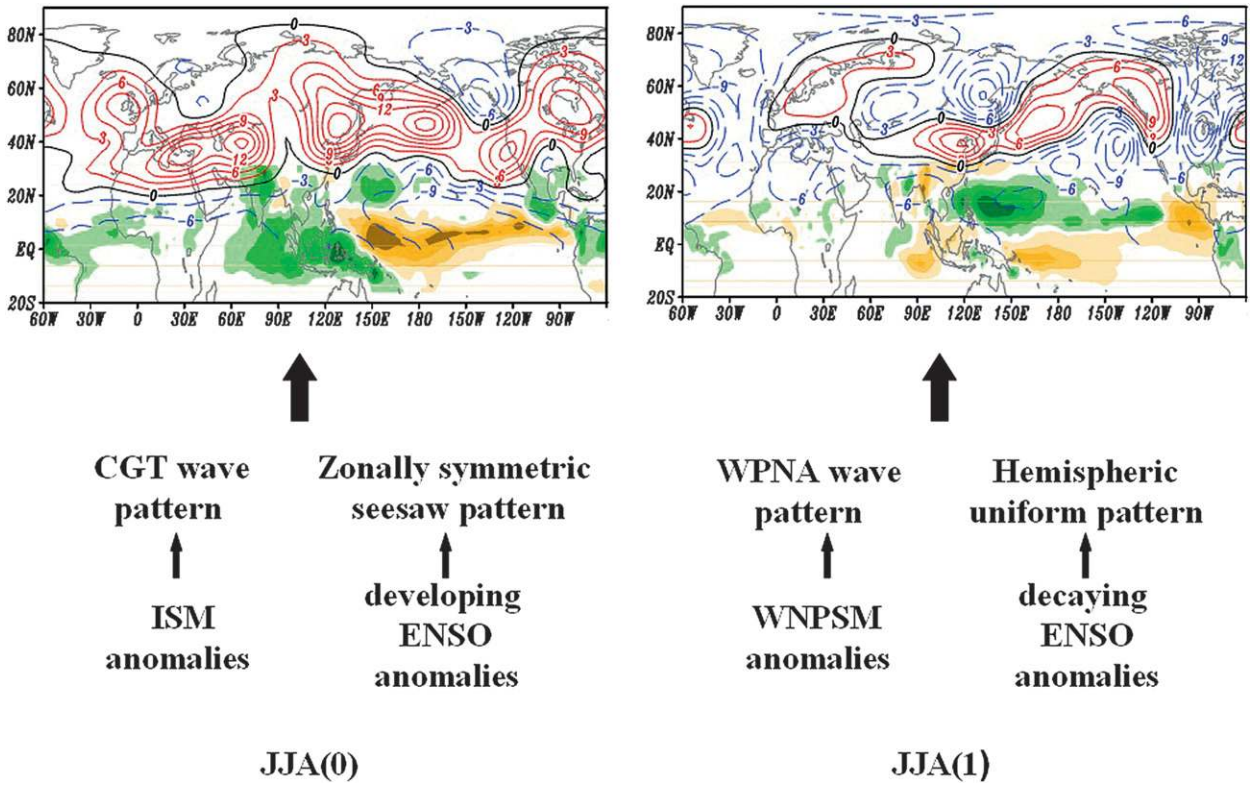

FIG. 11. Schematic showing the role of ENSO in organizing monsoon rainfall and the zonally symmetric and wave components of the boreal summer (JJA) circulation in year(0) and year(1). See section 8a for further details.

a great deal of similarity to the observed CGT. Not only is the dominant zonal wavenumber the same but so is the longitudinal phasing and latitudinal placement of the lobes. The one major failing is the weakness of the zonal-mean component—the same shortcoming that Branstator (2002) found when applying a similar methodology to the wintertime counterpart to the CGT.

Figures 10b and 10c show one-point correlation maps of 200-hPa streamfunction for the two major action centers of the EOF1 pattern in North America and the northeast Atlantic in the 1000 randomly forced solutions. The CGT-like wave train is clearly evident in these maps as well, another indication that linear processes—including wave propagation, refraction and reflection (Branstator 1983; Hoskins and Ambrizzi 1993), resonance (Hoskins and Karoly 1981; Held 1983), and barotropic energy conversion from the mean state to the perturbation flow (Simmons et al. 1983)—are sufficient to explain most features of the CGT pattern. Although the observational analysis in the previous section stressed that the CGT is the extratropical teleconnection pattern most closely linked with the tropical rainfall ''forcing,'' the linear solutions indicate that spatially organized forcing is unnecessary for producing the CGT pattern. This does not mean that local sources, including the ISM and ENSO, do not contribute to the excitation of the CGT, only that they do not need to be invoked to explain its characteristic structure and prominence.

8. Summary and implications for seasonal prediction

a. Summary

It is well known that ENSO can affect the NH circulation during the boreal winter. Here we have shown that it can also excite a strong extratropical circulation response in the boreal summer preceding the peak phase of an El Niño or La Niña event and a weaker, but sometimes detectable, response in the summer following the event. ENSO affects the extratropical circulation during the boreal summer by relocating the monsoonal heat sources.

Global-scale covariability between NH 200-hPa geopotential height (0°–87.5°N) and tropical rainfall (15°S–30°N) has been analyzed by applying MCA to a 62-yr-long dataset consisting of JJA means. This analysis yields a comprehensive picture of the global-scale tropical–extratropical teleconnections that reveals how tropical

heating anomalies force an NH extratropical response on the interannual time scale. Emphasis has been placed on assessing the role of the summer monsoons in mediating the response. In Fig. 11 we present a schematic diagram that highlights complementary roles of ENSO and monsoons in driving tropical–extratropical teleconnections during various phases of the ENSO cycle.

The leading MCA mode M1, which accounts for 47% of the squared covariance between tropical rainfall and NH 200-hPa height (Fig. 2a), links the CGT pattern with precipitation anomalies over Indian monsoon regions. The CGT is mainly confined within the waveguide associated with the westerly jet stream. The centers of action of the CGT tend to occur at preferred longitudes, as indicated in Fig. 2a, which are reproduced in the left-hand panel of Fig. 11. The second MCA mode M2, which explains another 25% of the squared covariance, reflects the relationship between summer rainfall anomalies in the WNPSM and the WPNA teleconnection pattern (Fig. 2b; right-hand panel of Fig. 11).

The extratropical circulation patterns in M1 and M2 closely resemble the leading EOFs of the NH upper-tropospheric circulation (Fig. 4). Both the CGT pattern (M1, EOF2) and the WPNA pattern (M2 and EOF1) exert a substantial impact on surface temperature over tropical and extratropical land areas (Fig. 3). The CGT pattern is linked to ISM variability, while the WPNA pattern is more connected with the WNPSM. The CGT explains most of interannual variability along the westerly jet. Thus, the CGT is the primary agent in conveying the influence of tropical thermal forcing to the NH extratropics.

M1 and M2 are associated with developing and decaying phases of extreme in the ENSO cycle, respectively (Fig. 5). The strong tropical SST anomalies observed during the summer preceding the peak phases of the ENSO cycle excite a strong extratropical response (Fig. 6a). In the summers following the peak phase of the ENSO cycle, ENSO-related rainfall anomalies are too weak to produce a robust extratropical response (Fig. 6b). The asymmetry between the strength of the extratropical patterns in the pre- and postpeak-phase summers is largely a reflection of the seasonality of the ENSO cycle itself and, in particular, the predictability barrier in the boreal spring.

The circulation patterns associated with M1 and M2 contain both zonally symmetric and zonally asymmetric components (Fig. 11). The wave components of the CGT and WPNA patterns are mainly related to the ISM and WNPSM forcing, respectively (Figs. 8 and 9). The zonally symmetric component exhibits a deep equivalent barotropic structure (Fig. 3). M1 is marked by an out-of-phase relationship between tropospheric temperature anomalies between the tropics and extratropics (Fig. 3a), while the zonally symmetric component of M2 tends to be spatially homogeneous throughout the tropical and extratropical NH (Fig. 3c). These zonally symmetric features exhibit a distinctive pattern of evolution in association with the ENSO cycle, with the tropical–extratropical seesaw prevailing in summers preceding the peak phase and the hemispheric uniform pattern prevailing in the summers following the peak phase (Fig. 7). Tropical and extratropical land surface temperatures vary in a similar manner.

We have shown evidence (Fig. 10) suggesting that linear, barotropic mechanisms, including energy propagation and barotropic instability of the midlatitude basic flow, shape the structure of the CGT and contribute to its prominence. Such internally generated extratropical variability can exist in the absence of tropical forcing but may also be excited by tropical forcing.

Our results suggest that three different factors are instrumental in producing tropical–extratropical teleconnections during the boreal summer: ENSO forces a zonally symmetric response in the tropics and extratropics, and it also modulates the rainfall in the ISM and other regional NH monsoons; the monsoons, in turn, act to excite the wave components of the CGT and WPNA patterns; and the internal dynamics of basic-state flow contributes to the characteristic structure of the CGT as well as to its maintenance.

b. Implications for seasonal prediction

The feasibility of seasonal climate prediction hinges on the premise that slowly varying boundary conditions at the earth's surface vary in a deterministic manner far beyond the limits of predictability of the atmospheric circulation alone (J. G. Charney and J. Shukla 1977, personal communication; Lorenz 1979; Shukla 1981). Seasonal prediction models based on this premise have had considerable success in predicting ENSO-related atmospheric circulation anomalies during the boreal winter. However, current models show very little skill in forecasting the NH extratropical summertime circulation, and this poses a major roadblock to operational use of the current seasonal prediction products (Wang et al. 2008). As noted above, the CGT and WPNA are closely related to tropical rainfall anomalies and thus could potentially be sources of predictability in forecasts of extratropical circulation anomalies. Realization of this predictability requires a predictive capability for tropical monsoon rainfall and an ability to accurately simulate the CGT and WPNA patterns. Simulating these patterns correctly requires that the model be able to faithfully simulate the boreal summer basic-state flow.

The existence of a boreal spring predictability barrier for ENSO may limit the degree to which the ENSO-related lead–lag relationships described in section 5 can be exploited in an operational setting. Developing El Niño and

La Niña events often first become recognizable between May and July—too late to provide much lead time for the JJA forecast for year 0 of the ENSO cycle, when the relationships involving M1 and the CGT are strong. A year 1 JJA forecast could be issued 6 months or more in advance, but lead–lag relationships to M2 and the WPNA pattern are relatively weak because of the boreal spring predictability barrier. Despite these limitations, it seems likely that JJA forecasts made at or just prior to the summer may have some skill, especially in years in which the SST anomalies at that time are appreciable and project in the patterns of year 0 or year 1 of the ENSO cycle.

To confirm the mechanisms proposed in this observational analysis will require a comprehensive numerical investigation involving a quantitative evaluation of the effects of the ISM, WNPSM, and ENSO on the extratropics and the modes of internal variability of the basic-state flow. Results of such an investigation are in progress and will be reported on in a subsequent article.

Acknowledgments. This study has been supported by the National Science Foundation's Climate Dynamics Program Awards ATM-0647995 (Ding and Wang) and 0812802 (Wallace), and NOAA's Climate Prediction Program for the Americas Award NA09OAR4310187 (Branstator).

APPENDIX

Barotropic Model

The equation of nondivergent barotropic model can be written as

$$\frac{\partial \zeta'}{\partial t} + \overline{\mathbf{v}_\psi} \cdot \nabla \zeta' + \mathbf{v}'_\psi \cdot \nabla \overline{\zeta} = f' - (\gamma + K\nabla^4)\zeta', \qquad \text{(A1)}$$

where $\overline{\zeta}$ and ζ' are the basic state and perturbation absolute vorticity, respectively; $\overline{\mathbf{v}_\psi}$ and $\mathbf{v}'_\psi$ denote the basic state and perturbation rotational horizontal velocity, respectively; and f' denotes externally prescribed stationary forcing. The model includes a linear damping rate of $(15 \text{ day})^{-1}$, which represents Rayleigh friction. The scale-selective biharmonic diffusion coefficient K is specified, so that the e-folding time scale of the smallest-scale eddies resolved in the model is 1 day. We spectrally transform Eq. (A1) in the horizontal at rhomboidal wavenumber 42, and the steady solutions are solved using the matrix inversion in the 1000 noise-forced experiment. To emphasize the wavy component of the response, the zonal mean component of the model response is removed in the analysis.

REFERENCES

Balmaseda, M., D. L. T. Anderson, and M. K. Davey, 1994: ENSO prediction using a dynamical ocean model coupled to statistical atmospheres. *Tellus,* **46A,** 497–511.

Barnston, A. G., and R. E. Livezey, 1987: Classification, seasonality and persistence of low-frequency atmospheric circulation patterns. *Mon. Wea. Rev.,* **115,** 1083–1126.

——, and Coauthors, 1994: Long-lead seasonal forecasts—Where do we stand? *Bull. Amer. Meteor. Soc.,* **75,** 2097–2114.

Blackburn, M., J. Methven, and N. Roberts, 2008: Large-scale context for the UK floods in summer 2007. *Weather,* **63,** 280–288.

Branstator, G., 1983: Horizontal energy propagation in a barotropic atmosphere with meridional and zonal structure. *J. Atmos. Sci.,* **40,** 1689–1708.

——, 1990: Low-frequency patterns induced by stationary waves. *J. Atmos. Sci.,* **47,** 629–649.

——, 2002: Circumglobal teleconnections, the jet stream waveguide, and the North Atlantic Oscillation. *J. Climate,* **15,** 1893–1910.

Bretherton, C. S., C. Smith, and J. M. Wallace, 1992: An intercomparison of methods for finding coupled patterns in climate data. *J. Climate,* **5,** 541–560.

Burgers, G., and D. B. Stephenson, 1999: The ''normality'' of El Ninõ. *Geophys. Res. Lett.,* **26,** 1027–1030.

Chen, M., P. Xie, J. E. Janowiak, and P. A. Arkin, 2002: Global land precipitation: A 50-yr monthly analysis based on gauge observations. *J. Hydrometeor.,* **3,** 249–266.

——, ——, ——, ——, and T. M. Smith, 2004: Verifying the reanalysis and climate models outputs using a 56-year data set of reconstructed global precipitation. Preprints, *14th Conf. on Applied Climatology,* Seattle, WA, Amer. Meteor. Soc., J6.1. [Available online at http://ams.confex.com/ams/84Annual/techprogram/paper_70083.htm.]

Chen, T. C., 2002: A North Pacific short-wave train during the extreme phases of ENSO. *J. Climate,* **15,** 2359–2376.

Chen, W. Y., 1982: Fluctuations in Northern Hemisphere 700 mb height fields associated with the Southern Oscillation. *Mon. Wea. Rev.,* **110,** 808–823.

Ding, Q.-H., and B. Wang, 2005: Circumglobal teleconnection in the Northern Hemisphere summer. *J. Climate,* **18,** 3483–3505.

——, and ——, 2007: Intraseasonal teleconnection between the summer Eurasian wave train and the Indian monsoon. *J. Climate,* **20,** 3751–3767.

——, and ——, 2009: Predicting extreme phases of the India summer monsoon. *J. Climate,* **22,** 346–363.

Enomoto, T., B. J. Hoskins, and Y. Matsuda, 2003: The formation mechanism of the Bonin high in August. *Quart. J. Roy. Meteor. Soc.,* **129,** 157–178.

Goswami, B. N., and J. Shukla, 1991: Predictability of the coupled ocean–atmosphere model. *J. Climate,* **4,** 3–22.

Held, I., 1983: Stationary and quasi-stationary eddies in the extratropical troposphere: Theory. *Large-Scale Dynamical Processes in the Atmosphere,* Academic Press, 127–168.

Hoerling, M. P., and A. Kumar, 2003: The perfect ocean for drought. *Science,* **299,** 691–694.

——, ——, J. S. Whitaker, and W. Wang, 2001: The midlatitude warming during 1998-2000. *Geophys. Res. Lett.,* **28,** 755–758.

Horel, J., 1981: A rotated principal component analysis of the interannual variability of the Northern Hemisphere 500-mb height field. *Mon. Wea. Rev.,* **109,** 2080–2092.

Hoskins, B. J., and D. J. Karoly, 1981: The steady linear response of a spherical atmosphere to thermal and orographic forcing. *J. Atmos. Sci.,* **38,** 1179–1196.

——, and T. Ambrizzi, 1993: Rossby wave propagation on a realistic longitudinally varying flow. *J. Atmos. Sci.,* **50,** 1661–1671.

Joseph, P. V., and J. Srinivasan, 1999: Rossby waves in May and the Indian summer monsoon rainfall. *Tellus,* **51A,** 854–864.

Kalnay, E., and Coauthors, 1996: The NCEP/NCAR 40–Year Reanalysis Project. *Bull. Amer. Meteor. Soc.,* **77,** 437–471.

Karoly, D. J., 1989: Southern Hemisphere circulation features associated with El Niño-Southern Oscillation events. *J. Climate,* **2,** 1239–1252.

Kumar, A., and M. P. Hoerling, 2003: The nature and causes for the delayed atmospheric response to El Niño. *J. Climate,* **16,** 1391–1403.

——, W. Wang, M. P. Hoerling, A. Leetmaa, and M. Ji, 2001: The sustained North American warming of 1997 and 1998. *J. Climate,* **14,** 345–353.

Latif, M., and Coauthors, 1998: A review of the predictability and prediction of ENSO. *J. Geophys. Res.,* **103,** 14 375–14 393.

Lau, K.-M., 1992: The East Asian summer monsoon rainfall variability and climate teleconnection. *J. Meteor. Soc. Japan,* **70,** 211–241.

——, and L. Peng, 1992: Dynamics of atmospheric teleconnections during the northern summer. *J. Climate,* **5,** 140–158.

——, and H.-Y. Weng, 2002: Recurrent teleconnection patterns linking summertime precipitation variability over East Asia and North America. *J. Meteor. Soc. Japan,* **80,** 1309–1324.

Lau, N.-C., and M. J. Nath, 2003: Atmosphere–ocean variations in the Indo-Pacific sector during ENSO episodes. *J. Climate,* **16,** 3–20.

——, A. Leetmaa, M. J. Nath, and H.-L. Wang, 2005: Influences of ENSO-induced Indo–Western Pacific SST anomalies on extratropical atmospheric variability during the boreal summer. *J. Climate,* **18,** 2922–2942.

Li, S., J. Perlwitz, X. Quan, and M. P. Hoerling, 2008: Modelling the influence of North Atlantic multidecadal warmth on the Indian summer rainfall. *Geophys. Res. Lett.,* **35,** L05804, doi:10.1029/2007GL032901.

Lin, H., 2009: Global extratropical response to diabatic heating variability of the Asian summer monsoon. *J. Atmos. Sci.,* **66,** 2697–2713.

Livezey, R. E., and W.-Y. Chen, 1983: Statistical field significance and its determination by Monte Carlo techniques. *Mon. Wea. Rev.,* **111,** 46–59.

Lorenz, E. N., 1979: Forced and free variations of weather and climate. *J. Atmos. Sci.,* **36,** 1367–1376.

Lu, R.-Y., J.-H. Oh, and B.-J. Kim, 2002: A teleconnection pattern in upper-level meridional wind over the North African and Eurasian continent in summer. *Tellus,* **54A,** 44–55.

Mitchell, T. D., and P. D. Jones, 2005: An improved method of constructing a database of monthly climate observations and associated high-resolution grids. *Int. J. Climatol.,* **25,** 693–712, doi:10.1002/joc.1181.

Nitta, T., 1987: Convective activities in the tropical western Pacific and their impact on the Northern Hemisphere summer circulation. *J. Meteor. Soc. Japan,* **65,** 373–390.

Parthasarathy, B., A. A. Munot, and D. R. Kothawale, 1994: All-India monthly and seasonal rainfall series 1871-1993. *Theor. Appl. Climatol.,* **49,** 217–224.

Rajeevan, M., and L. Sridhar, 2008: Inter-annual relationship between Atlantic sea surface temperature anomalies and Indian summer monsoon. *Geophys. Res. Lett.,* **35,** L21704, doi:10.1029/2008GL036025.

Rasmusson, E. M., and T. H. Carpenter, 1982: Variations in tropical sea surface temperature and surface wind fields associated with the Southern Oscillation/El Niño. *Mon. Wea. Rev.,* **110,** 354–384.

Schubert, S. D., M. J. Suarez, P. J. Pegion, M. A. Kistler, and A. Kumar, 2002: Predictability of zonal means during boreal summer. *J. Climate,* **15,** 420–434.

Seager, R., N. Harnik, Y. Kushnir, W. Robinson, and J. Miller, 2003: Mechanisms of hemispherically symmetric climate variability. *J. Climate,* **16,** 2960–2978.

Shukla, J., 1981: Dynamical predictability of monthly means. *J. Atmos. Sci.,* **38,** 2547–2572.

——, and D. A. Paolino, 1983: The Southern Oscillation and long-range forecasting of the summer monsoon rainfall over India. *Mon. Wea. Rev.,* **111,** 1830–1837.

Sikka, D. R., 1980: Some aspects of the large scale fluctuations of summer monsoon rainfall over India in relation to fluctuations in the planetary and regional scale circulation parameters. *J. Earth Syst. Sci.,* **89,** 179–195.

Simmons, A. J., J. M. Wallace, and G. W. Branstator, 1983: Barotropic wave propagation and instability, and atmospheric teleconnection patterns. *J. Atmos. Sci.,* **40,** 1363–1392.

Smith, T. M., R. W. Reynolds, T. C. Peterson, and J. Lawrimore, 2008: Improvements to NOAA's historical merged land–ocean surface temperature analysis (1880–2006). *J. Climate,* **21,** 2283–2296.

Ting, M., and H. Wang, 1997: Summertime U.S. precipitation variability and its relation to Pacific sea surface temperature. *J. Climate,* **10,** 1853–1873.

Torrence, C., and P. J. Webster, 1998: The annual cycle of persistence in the El Niño–Southern Oscillation. *Quart. J. Roy. Meteor. Soc.,* **124,** 1985–2004.

Trenberth, K. E., and G. W. Branstator, 1992: Issues in establishing causes of the 1988 drought over North America. *J. Climate,* **5,** 159–172.

——, and C. J. Guillemot, 1996: Physical processes involved in the 1988 drought and 1993 floods in North America. *J. Climate,* **9,** 1288–1298.

——, G. W. Branstator, and P. A. Arkin, 1988: Origins of the 1988 North American drought. *Science,* **242,** 1640–1645.

Wallace, J. M., and D. S. Gutzler, 1981: Teleconnection in the geopotential height field during the Northern Hemisphere winter. *Mon. Wea. Rev.,* **109,** 784–812.

——, C. Smith, and C. S. Bretherton, 1992: Singular value decomposition of wintertime sea surface temperature and 500-mb height anomalies. *J. Climate,* **5,** 561–576.

Wang, B., R. Wu, and X. Fu, 2000: Pacific–East Asian teleconnection: How does ENSO affect East Asian climate? *J. Climate,* **13,** 1517–1536.

——, ——, and K.-M. Lau, 2001: Interannual variability of the Asian summer monsoon: Contrasts between the Indian and the western North Pacific–East Asian monsoons. *J. Climate,* **14,** 4073–4090.

——, and Coauthors, 2008: Advance and prospectus of seasonal prediction: Assessment of the APCC/CliPAS 14-model ensemble retroperspective seasonal prediction (1980–2004). *Climate Dyn.,* **30,** 605–619.

Wilks, D. S., 1995: *Statistical Methods in the Atmospheric Sciences: An Introduction*. Academic Press, 467 pp.

Xue, Y., M. A. Cane, S. E. Zebiak, and M. B. Blumenthal, 1994: On the prediction of ENSO—A study with a low-order Markov model. *Tellus,* **46A,** 512–528.

Yadav, R. K., 2009a: Changes in the large-scale features associated with the Indian summer monsoon in the recent decades. *Int. J. Climatol.,* **29,** 117–133.

——, 2009b: Role of equatorial central Pacific and northwest of North Atlantic 2-metre surface temperatures in modulating Indian summer monsoon variability. *Climate Dyn.,* **32,** 549–563.

Yang, J., Q. Liu, Z. Liu, L. Wu, and F. Huang, 2009: Basin mode of Indian Ocean sea surface temperature and Northern Hemisphere circumglobal teleconnection. *Geophys. Res. Lett.,* **36,** L19705, doi:10.1029/2009GL039559.

Yasui, S., and M. Watanabe, 2010: Forcing processes of the summertime circumglobal teleconnection pattern in a dry AGCM. *J. Climate,* **23,** 2093–2114.

Yulaeva, E., and J. M. Wallace, 1994: The signature of ENSO in global temperature and precipitation fields derived from the microwave sounding unit. *J. Climate,* **7,** 1719–1736.